Materials & Design 214 (2022) 110387

Contents lists available at ScienceDirect

Materials & Design

journal homepage: www.elsevier.com/locate/matdes

An optimisation method for the cold-spray process: On the nozzle geometry

L. Alonso *, M.A. Garrido, P. Poza

Department of Chemical Technology, Energy and Mechanics, Rey Juan Carlos University, C/Tulipán s.n., 28933, Spain

HIGHLIGHTS

- The analytical model is able to predict the optimal nozzle geometry under certain stagnation conditions.
- Some of the typical hypotheses of these simplified fluid-dynamics models are improved.
- A geometric criterion based on the current designs is defined for the optimal geometry.
- The relative influence of different parameters on the nozzle geometry is studied.

GRAPHICAL ABSTRACT

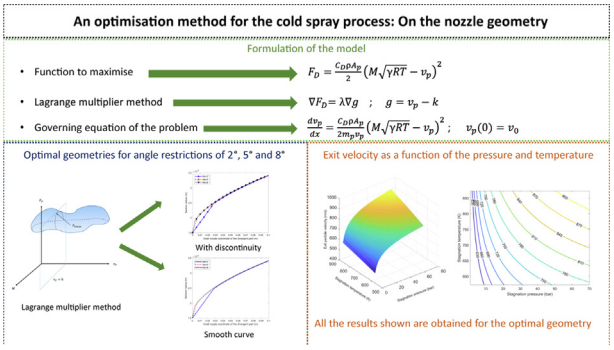

ARTICLE INFO

Article history:
Received 10 September 2021
Revised 23 December 2021
Accepted 5 January 2022
Available online 08 January 2022

Keywords:
Cold spray
Optimisation
Analytical modelling
Nozzle geometry

ABSTRACT

Currently, the cold-spray process, or simply cold spray, is an extensively used technique in coating applications. The low temperature of the deposition process is the distinctive feature that makes it suitable for many additive manufacturing activities such as repair and restoration of damaged components. The reliability of the coatings is strongly dependent on the velocity of the powder during its impact on the target surface. Spraying conditions such as the pressure and temperature of the carrier gas and the geometry of the nozzle control the acceleration of the powder particles. Consequently, there is an increasing interest in the optimisation of nozzle geometry so as to maximise the acceleration of the particles through the nozzle path that they follow. In contrast with various extant approaches to achieve this aim (finite element modelling, experimental approach, and analytical methods), an alternative model based on the one-dimensional isentropic theory that accounts for the dynamics of the dilute two-phase flow was developed in this study. First, an analysis of the common hypotheses used to obtain the equation of motion of the particle was carried out. Subsequently, with the new insights revealed from the previous analysis, a new theoretical model for the optimisation of the divergent part of the nozzle was performed considering a geometric angle restriction. This model is based on the numerical integration of the equation of motion of the particle, ensuring the maximisation of the particle drag force by means of the Lagrange multiplier method. Once the analytical model is formulated, a set of curves describing the optimal geometric parameters for different conditions is obtained. Moreover, some optimal geometries are presented demonstrating the low influence of the angle restriction. Additionally, the inversely proportional relationship between stagnation pressure and temperature is revealed.

* Corresponding author.
E-mail address: luis.alonso.sanjose@urjc.es (L. Alonso).

https://doi.org/10.1016/j.matdes.2022.110387
0264-1275/

1. Introduction

The cold-spray process is a dynamic technique for material deposition in which fine, solid powder particles are accelerated to a supersonic velocity in the range of 500–1200 m/s dragged by a compressed carrier gas. During the deposition process, the temperature of the particles remains below the melting temperature of the materials [2]. Therefore, the deposition mechanism is a solid-state process. The procedure by which the particles bond onto the substrate and among themselves is controlled by their plastic deformation during the impact. A threshold deformation value should be achieved by the sprayed particles to guarantee intimate contact with the target surface. Consequently, a threshold value of the particle kinetic energy or particle impact velocity should be overcome to promote bonding. Experimental observations indicate that maximising the impact velocities of the sprayed particles can result in a successful deposition [10]. Moreover, the powder particles should be accelerated above a threshold velocity, often referred to as "critical velocity," to achieve acceptable deposition efficiencies. This velocity is influenced by the mechanical properties of the sprayed material and substrate, and the particle properties, such as size and temperature [11,30,9,3,12,17]. For many ductile materials such as metal alloys, the critical velocity is above 700 m/s [1]. It has also been reported that the critical velocity decreases when the temperature of the particles increases. Consequently, the deposition efficiency may also be improved by increasing the particle temperature [9]. In a cold spray, the particles gain speed in a supersonic gas flow which is achieved by introducing a compressed, preheated gas into a converging-diverging nozzle. In addition, the converging/diverging geometry of the nozzle itself should be optimised to maximise the particle velocity. The gas velocity increases in the diverging section of the nozzle owing to expansion while the gas temperature rapidly decreases. In this section, the particles gain a substantial speed. To maximise the particle impact velocity, cold-spray nozzles are designed to maintain supersonic gas flow inside the diverging section [10,19]. For this reason, in several cold-spray equipment, the particles are added to the gas flow before the converging section of the nozzle. Several studies have been performed to model the fluid dynamics inside a nozzle. Computational fluid dynamics (CFD) is a powerful tool for determining the particle and gas velocities and temperatures throughout the nozzle [28,29,13,22,6]. Dykhuizen and Smith [10] presented an analytical model of the cold-spray process assuming a one-dimensional (1D) isentropic flow and constant gas properties. Under this simplification, the velocity of the particle could be predicted by solving a differential equation derived on the basis of Newton's second law. The analytical results allowed for the determination of an optimal design for a cold-spray nozzle. The solutions demonstrated that the spray particle velocity is a function of the spraying conditions, such as carrier gas, particle material density, and particle size. It also depends on the geometric dimensions of the nozzle. They reported that the particle velocity is influenced by the nozzle length but is not sensitive to the nozzle shape. The analytical solution proposed by Dykhuizen and Smith [10] was derived under the conditions of constant gas velocity, gas density, and drag coefficient. However, this assumption may provide analytical results that are significantly different from the actual behaviour during the spraying process [14,12,33]. Assadi et al. [4] developed a series of parameters to predict particle impact velocities based upon the initial input conditions. They numerically solved the force balance differential equation to calculate the particle velocity of a spherical shape. A 1D isentropic model of gas flow through a convergent–divergent nozzle was considered, and the nozzle was assumed to have a linear profile with a conical shape in both the convergent and divergent parts. They found that the main coating characteristics can be described as a unique function of the ratio of particle velocity to critical velocity. The solution of the force balance equation was obtained by assuming that some parameters such as the gas density and temperature were variable while others such as the drag coefficient were constant. The aspect of nozzle design have been widely investigated using more complete three-dimensional computational CFD models [18,19,12]. Vadla and Doom [31] analysed the jet characteristics of various geometries of the cold-spray nozzles. They compared step-drilled, conical, and curved shapes using CFD numerical simulations by solving the Navier-Stokes equations. They concluded that a curved nozzle resulted in a slightly higher exit velocity, which may be further enhanced by optimising the nozzle length. Samareh and Dolatabadi [25,26] performed simulations using a full three-dimensional model to determine the optimal nozzle position and substrate shape as well as the effect of particle flow density. They found that three-dimensional analysis helps elucidate the complex gas and particle flow fields generated by the particle injection process. In addition, this analysis enables the investigation of the effect of substrate shapes (i.e. convex and concave) on the flow field and, consequently, to determine the optimum conditions for depositing coating particles. Three-dimensional CFD simulations provide design solutions that minimise the simplifications and assumptions commonly imposed in analytical studies. However, the determination of the interactions and influence of the different spray parameters on the nozzle design is very complex. In addition, the computational time of these simulations was significantly higher than the time required to solve the simplified analytical models. Consequently, this study aimed to develop a theoretical model for the optimisation of the geometry of the divergent part of the nozzle so as to ensure the maximum velocity of the particles at the nozzle exit. To this end, and in contrast with previous studies, a 1D isentropic model of gas flow through a convergent–divergent nozzle was numerically solved considering variations in the gas velocity, gas density, gas temperature, gas dynamic viscosity, and drag coefficient during the flow through the nozzle. A subsequence comparison between this numerical solution and a previously proposed analytical solution [10], with the afore described simplifications incorporated, enabled the observation of discrepancies between both alternatives. Finally, the numerical solution was coupled with a user-defined geometric criterion, and the optimal values of the nozzle geometric parameters under different spraying conditions were obtained; this is a novel aspect of this study.

2. Study of the hypotheses assumed in the particle motion

2.1. Particle motion models

It is widely assumed that the solid phase related to the powder in a cold-spray process can be considered sufficiently dilute to move along the nozzle axis with no other force acting than the drag force induced by the fluid [12,33]. Under this assumption, Newton's second law provides a differential equation to obtain the velocity of the particle along the nozzle axis:

$$m_p \frac{dv_p}{dt} = \frac{C_D \rho A_p}{2} (v - v_p)^2 \tag{1}$$

where m_p, C_D, ρ, A_p, v and v_p are the average mass of the particle, drag coefficient, gas density, average projected area of the particle, gas velocity, and particle velocity, respectively. Further, equation (1) may be expressed in terms of the axial nozzle coordinate, x, using the chain rule:

$$\frac{dv_p}{dt} = \frac{dv_p}{dx} v_p \tag{2}$$

Some authors consider the drag coefficient C_D as a constant [15,33]. Nevertheless, there are other more realistic approaches that consider the dependency between the drag coefficient and relative Reynolds number [7,12]. In this study, the correlation provided by Clift et al. [7], which holds for incompressible and compressible fluids, was used.

$$C_D = \frac{24}{Re_p}\left(1 + 0.15Re_p^{0.687}\right) + \frac{0.42}{1 + 4.25e4Re_p^{-1.16}} \tag{3}$$

where Re_p is the relative Reynolds number defined as,

$$Re_p = \frac{\rho d_p (v - v_p)}{\mu} \tag{4}$$

where μ is the dynamic viscosity of the fluid, and d_p is the average diameter of the metal powder. In contrast with the common approach of considering the dynamic viscosity constant, several studies have shown significant differences (one order of magnitude) in the typical range of temperatures during the cold spray process, that is, from 473 K to 1373 K [32,20]. In this regard, Sutherland's law predicts the dynamic viscosity change for a gas with temperature, which is described as follows:

$$\mu = \mu_0 \frac{T_0 + C_s}{T + C_s}\left(\frac{T}{T_0}\right)^{\frac{3}{2}} \tag{5}$$

where C_s is the Sutherland constant, and μ_0 is the dynamic viscosity of the reference at a certain temperature T_0. The dependence of the dynamic viscosity on the pressure has been scarcely studied. Nevertheless, there is a general consensus on the independence of dynamic viscosity up to a certain pressure. In the typical range of pressures used in the cold-spray process (approximately 1–70 bar), the dependence of viscosity on pressure can be neglected [20].

It is interesting to highlight the dependencies of the gas density, pressure, temperature, and velocity with the Mach number. Under the assumption of 1D isentropic flow, the following well-known relationships (equations (6)–(12)) are obtained [15,12,33]:

$$\frac{P_0}{P} = \left[1 + \frac{\gamma - 1}{2}M^2\right]^{\frac{\gamma}{\gamma - 1}} \tag{6}$$

where P, P_0, γ, and M are the pressure, stagnation pressure, relationship between the isobaric gas heat capacity, isochor-specific gas heat capacity, and the Mach number, respectively;

$$\frac{T_0}{T} = 1 + \frac{\gamma - 1}{2}M^2 \tag{7}$$

where T and T_0 are the temperature and stagnation temperature, respectively;

$$\frac{\rho_0}{\rho} = \left[1 + \frac{\gamma - 1}{2}M^2\right]^{\frac{1}{\gamma - 1}} \tag{8}$$

where ρ and ρ_0 are the density and stagnation density, respectively;

$$v = M\sqrt{\gamma RT} \tag{9}$$

where R is the gas constant in the ideal gas law. This law couples the gas pressure, density, and temperature through the gas constant, as expressed in equation (10),

$$P = \rho RT \tag{10}$$

All the previously defined quantities are necessary to solve equation (1). They can be determined if the Mach number is known for each spatial axial nozzle coordinate. Fortunately, there is a relationship that couples the Mach number with the nozzle cross-sectional area; thus, if the geometry is known, the Mach number can be determined as follows:

$$\frac{A}{A*} = \frac{1}{M}\left[\left(\frac{1}{\gamma + 1}\right)\left(1 + \frac{\gamma - 1}{2}M^2\right)\right]^{\frac{\gamma + 1}{2(\gamma - 1)}} \tag{11}$$

where A is the cross-sectional area, and $A*$ is the cross-sectional area of the nozzle throat. In case of the simplified models, equation (1) is frequently solved in prior studies under strong assumptions [15,12,33]. If the gas velocity, gas density, gas temperature, and drag coefficient are assumed to be constants, equation (1) can be easily integrated to provide an implicit expression between the particle velocity and position.

$$\log\left(\frac{v - v_p}{v}\right) + \frac{v}{v - v_p} - 1 = \frac{C_D A_p \rho}{2m_p}x \tag{12}$$

Equation (12) provides a rough estimation of the particle velocity with position. Therefore, the next step is to establish the range within which these strong simplifications are valid.

2.2. Comparison between the simplified and the fully integrated model

This section concerns the variations in the gas velocity, density, temperature, dynamic viscosity, and drag coefficient during travel through the nozzle, which significantly affect the final velocity. The other approach proposed herein to consider these variations is to numerically integrate equation (1) and introduce the corresponding expressions that vary with the Mach number and, thus, with the axial position along the nozzle. To elucidate the differences between the particle velocities through the nozzle and the final particle velocities, the two models were analysed by means of two different geometries and stagnation conditions. As this section details purely mathematical aspects, in order to examine the implications of the hypotheses, the nozzle geometries used to compare both models are two paraboloids with diameters and length within the typical range [24,21,31], as shown in Fig. 1.

Because of its good performance and extended use [21], nitrogen gas was selected to carry out a comparison between both models. Aluminium was used for the powder because of its versatility with respect to the deposition conditions. Furthermore, an average particle diameter of 10 μm was used for all the simulations. In order to investigate the differences between the simplified and fully integrated models, the two most accessible parameters in the cold-spray equipment were analysed— stagnation pressure and temperature. The particle velocity for the two models is represented in Fig. 2 as a function of the axial nozzle coordinate at a

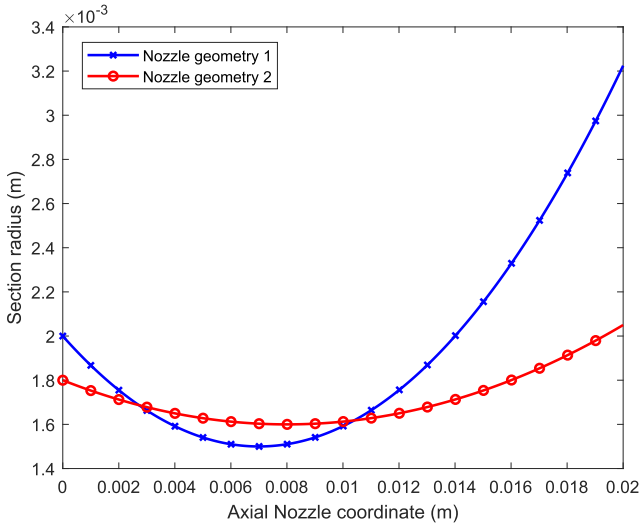

Fig. 1. Section radius versus the axial nozzle coordinate for the two geometries proposed.

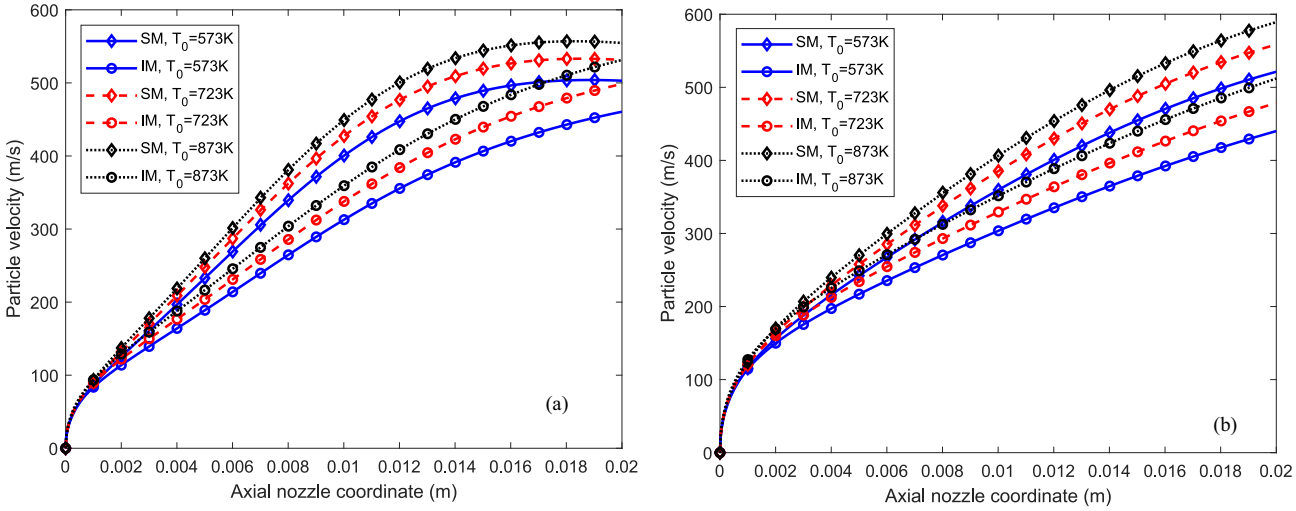

Fig. 2. Particle velocity versus the axial nozzle coordinate for geometries (a) 1 and (b) 2 for different temperatures, comparison between the simplified model (SM) and the fully integrated model (IM), at a constant pressure of 30 bar.

constant pressure of 30 bar [8,16] for the following three different stagnation temperatures: 573 K [16], 723 K [23], and 873 K, which was chosen as the upper limit near the melting temperature.

As shown in Fig. 2, the differences between the particle velocities along the axial nozzle coordinate predicted by the simplified model (SM) and fully integrated model (IM) are not negligible. The particle velocity increased in both models with stagnation temperature. Generally, SM overestimates the particle velocity for all analysed cases. The main objective of these models is to predict the final particle velocity. The differences in the prediction of these parameters are below 10% for the first geometry. Nevertheless, these discrepancies are greater for the second geometry, reaching values above 18%. Furthermore, the differences in the final velocities tended to decrease with increasing stagnation temperature. Fig. 3 shows the particle velocity versus the axial nozzle coordinate at a constant temperature of 723 K [23] for three different stagnation pressures: 4 bar, which was selected as the lower limit of low pressure, 30 bar [8,16] and 60 bar [27], representing the low, medium and high pressure respectively. Fig. 3a and 3b present the results for both models for the first proposed geometry and the second proposed geometry, respectively.

Fig. 3 depicts remarkable differences between the predictions of the particle velocities using the SM and IM models. The particle velocity increases in both models with the stagnation pressure. As can be observed in Fig. 2 the SM overestimates the particle velocities for all the cases analysed. In contrast with the behaviour observed in Fig. 2 the differences in the final particle velocity increases when increasing stagnation pressure in both models for the two geometries studied. The differences in the final particle velocities are greater for the second geometry Fig. 3b, being above 17% for the 60 bar pressure case.

These results indicate that the SM accurately predicted the final particle velocity for some conditions of stagnation temperature and pressure. It is adequate at low pressures and high temperatures. The differences along the axial nozzle coordinate are never negligible; however, the most important result is the exit particle velocity. Nonetheless, the errors resulting under certain conditions ($P_0 = 30$ bar,$T_0 = 573$ K or $P_0 = 60$ bar, $T_0 = 723$ K) are not acceptable. Thus, it is reasonable to use the IM to minimise the prediction errors. In addition, the accuracy of the SM strongly depends on the nozzle geometry, as shown in Figs. 2 and 3 Therefore, IM was used thereafter in this study, as detailed in subsequent

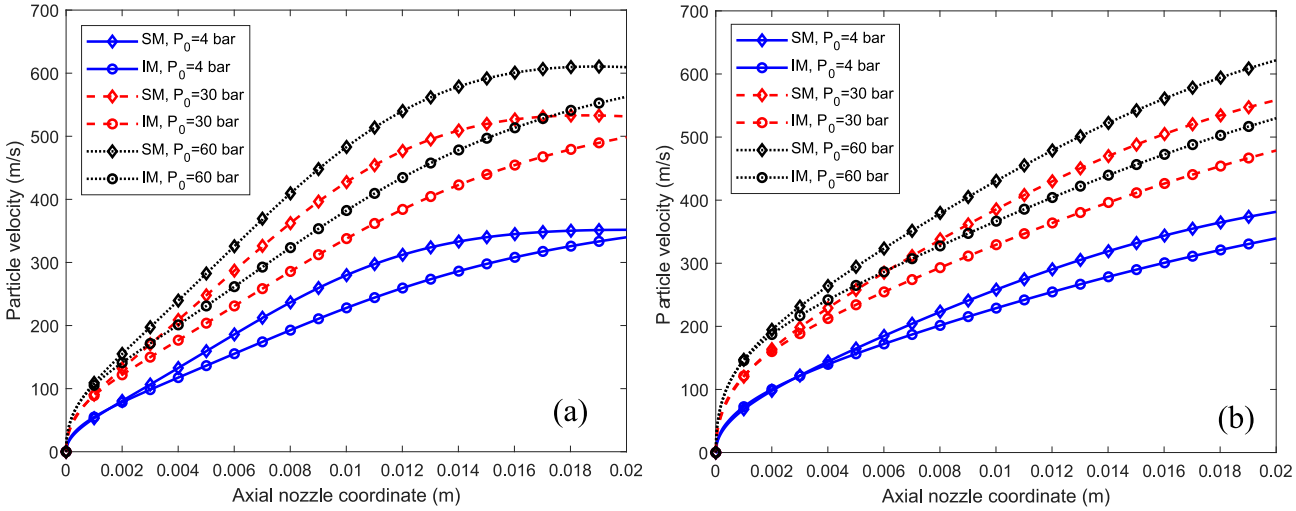

Fig. 3. Particle velocity versus the axial nozzle coordinate for geometries (a) 1 and (b) 2 for different pressures, comparison between the simplified model (SM) end the full integrated model (IM), at a constant temperature of 723 K.

sections. Furthermore, each axial nozzle coordinate is important for optimisation.

3. Study of the hypotheses assumed in the particle motion

Analytical models for the optimisation of the divergent and convergent parts of the nozzle are available in the literature [12,34,5]. These models are usually focused on the optimisation of the Mach number that maximises the drag force acting on the particle to obtain the optimal area using equation (11). This paper presents a new methodology based on the Lagrange multiplier method coupled with a user-defined geometrical criterion in order to obtain the optimal geometry of the divergent part of the nozzle. The function to maximise in each step of spatial integration is the drag force, v_p, acting on the particle, that is, the right-hand side of equation (1). The combination of equations (1) and (9) provides the function to be maximised in terms of only two independent variables v_p and M,

$$F_D = \frac{C_D \rho A_p}{2}\left(M\sqrt{\gamma RT} - v_p\right)^2 \tag{13}$$

Because the IM needs to be numerically integrated (equation (1)), the Mach number that maximises the drag force (13) must be determined at each step of the spatial integration. During each integration step, the particle velocity remains constant. This restriction is used to determine the maximum in equation (13). The procedure followed for solving the optimisation problem starts with the conditions that are known at the nozzle throat because the convergent part is determined. With these initial conditions, equation (1) is solved. For each integration step, the Mach number that maximises the drag force (equation (13)) is calculated using the model described below. When the integration is completed, the particle velocity and the optimal Mach number are known at each coordinate; thus, the optimal area can be determined using equation (11). The equations used to determine the optimal Mach number with the Lagrange multiplier technique are as follows:

$$\nabla F_D = \lambda \nabla g \tag{14}$$

$$\nabla F_D = \left(\frac{\partial F_D}{\partial v_p}, \frac{\partial F_D}{\partial M}\right) \tag{15}$$

$$g = v_p - k \tag{16}$$

where λ is the Lagrange multiplier, g is the restriction of the problem, and k is the particle velocity at each integration step. The process for obtaining the optimal Mach number is illustrated in Fig. 4.

By developing equations (14), (15), and (16), the following system with three equations and three unknowns, λ, v_p, and M, is obtained:

$$\frac{A_p\rho}{2}\left[\frac{dC_D}{dRe_p}\frac{\partial Re_p}{\partial v_p}\left(M\sqrt{\gamma RT} - v_p\right)^2 - 2C_D\left(M\sqrt{\gamma RT} - v_p\right)\right] = \lambda \tag{17}$$

$$\begin{aligned}&\frac{dC_D}{dRe_p}\frac{\partial Re_p}{\partial M}\rho\left(M\sqrt{\gamma RT} - v_p\right)^2 \\ &+ C_D\left[\frac{d\rho}{dM}\left(M\sqrt{\gamma RT} - v_p\right)^2 + 2\rho\left(M\sqrt{\gamma RT} - v_p\right)\left[\sqrt{\gamma RT} + M\frac{\sqrt{\gamma RT}}{2T}\frac{dT}{dM}\right]\right] \\ &= 0\end{aligned} \tag{18}$$

$$v_p = k \tag{19}$$

Equation (18) was solved using the Newton–Raphson procedure. Notably, temperature and density, as well as their derivatives, depend only on the Mach number. The solution of these systems at each integration step provides the optimal Mach number. The derivatives related to the Reynolds number are defined as follows:

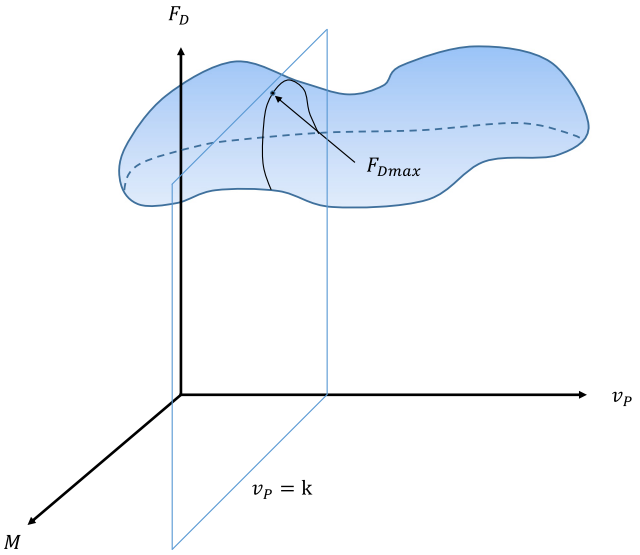

Fig. 4. Schematic representation for the determination of the optimal Mach number at each integration step by means of the Lagrange multiplier method.

$$\frac{dC_D}{dRe_p} = \frac{-24\left(0.04695Re_p^{0.687} + 1\right)}{Re_p^2} + \frac{2.0706e4Re_p^{-2.16}}{\left(1 + 4.25e4Re_p^{-1.16}\right)^2} \tag{20}$$

$$\frac{\partial Re_p}{\partial v_p} = -\frac{\rho d_p}{\mu} \tag{21}$$

$$\begin{aligned}\frac{\partial Re_p}{\partial M} = \frac{d_p}{\mu^2}&\left[\left[\frac{d\rho}{dM}\left(M\sqrt{\gamma RT} - v_p\right) + \rho\left(\sqrt{\gamma RT} + M\frac{\sqrt{\gamma RT}}{2T}\frac{dT}{dM}\right)\right]\mu\right. \\ &\left. - \rho\left(M\sqrt{\gamma RT} - v_p\right)\frac{d\mu}{dT}\frac{dT}{dM}\right]\end{aligned} \tag{22}$$

and the derivatives related to the gas properties, that is, temperature, density, and viscosity:

$$\frac{dT}{dM} = -T_0(\gamma - 1)M\left[1 + \frac{\gamma - 1}{2}M^2\right]^{-2} \tag{23}$$

$$\frac{d\rho}{dM} = -\rho_0 M\left[1 + \frac{\gamma - 1}{2}M^2\right]^{-\frac{\gamma}{\gamma - 1}} \tag{24}$$

$$\frac{d\mu}{dT} = \mu_0\left[-\frac{T_0 + C_s}{(T + C_s)^2}\left(\frac{T}{T_0}\right)^{\frac{3}{2}} + \frac{3}{2T_0}\left(\frac{T_0 + C_s}{T + C_s}\right)\left(\frac{T}{T_0}\right)^{\frac{1}{2}}\right] \tag{25}$$

The differential equation of particle motion, along with an initial condition, forms the governing equation of the problem considered herein.

$$\begin{aligned}&\frac{dv_p}{dx} = \frac{C_D\rho A_p}{2m_p v_p}\left(M\sqrt{\gamma RT} - v_p\right)^2 \\ &v_p(0) = v_0\end{aligned} \tag{26}$$

where v_0 denotes the particle velocity at the nozzle throat. Equation (26) combined with equations (17), (18), and (19) at each spatial integration yields the required solution. Nevertheless, there is a discontinuity associated with the condition $M = 1$ at the nozzle throat. Even though the model starts with $M = 1$, in the following step, the set of equations (17), (18), and (19) provides an optimal Mach

number that is considerably greater than unity. This would provoke a discontinuity in the divergent part (11) of the nozzle throat. To avoid this discontinuity, a geometrical criterion based on the manufacturing data available in the literature was proposed. A maximum divergent angle is fixed, and if equations (17), (18), and (19) provide an optimal Mach number resulting in a divergent angle (with equation (11) accounting for the previous coordinate) below the maximum angle, the Mach number provided by the Lagrange multiplier method is used. On the contrary, if the divergent angle is not within the established range, an additional restriction is imposed to obtain a range of the Mach number which meets the geometrical requirement. Thus, a geometrical discontinuity is avoided. In the next section, examples of optimal nozzle geometries for different geometrical conditions are presented.

4. Results

The optimisation model was validated by means of a comparison of its results with those from the commercial software ANSYS v.17. Subsequently, two sets of results were analysed. Different divergent nozzle geometries were obtained for a specific length and geometric constraints. A comparison between the mathematical and engineering solutions was performed by adding features that improved the projection response of the nozzle. In addition, an analysis using the classical conical divergent shape was performed to gain new insights into the utility of the model. Subsequently, various maps of interest to obtain the final particle velocity and optimal geometrical parameters were obtained. Finally, an analysis to reveal the influence of the particle size and material on the optimal geometry was performed. All simulations before the analysis of the particle size were performed with an average particle diameter of 10 μm.

4.1. Particle motion models

The optimal geometries obtained in this study are not commercially available; therefore, they cannot be compablue with experimental results. To ensure consistency with the results obtained from the numerical resolution of the equations that lead to the optimisation of the nozzle geometry, a CFD simulation was performed to study the flow inside the divergent section of the nozzle. The CFD simulation domain was oriented such that the X-direction was horizontal and parallel to the longitudinal axis of the nozzle and the predominant flow direction. The optimised geometry of the analytical solution was imported into the CFD software (ANSYS Fluent). A 2D axisymmetric simulation was proposed, taking advantage of the revolution symmetry of the problem. The symmetric axis was coincident with the X-direction. A convergent section was added to the imported geometry to analyse the behaviour of the fluid through the constriction from the convergent region to the divergent region. The computational domain was discretised using hexahedral brick elements. The characteristic element size was 0.2 mm. However, the characteristic length of the elements close to the constriction was reduced to 0.1 mm in order to increase the accuracy and avoid convergence problems. The fluid selected was nitrogen, which is an ideal gas with a molecular weight of 28.0134 g/mol, and a piecewise polynomial function for its specific heat was selected from the database of the CFD software. The values of the pressure and temperature imposed in the inlet section of the convergent part were 15.85 bars and 603 K, respectively. These values were equal to those obtained in the analytical solution. The values of the flow velocity and Mach number along the longitudinal axis of the nozzle were obtained from CFD simulations. An example of the simulation is shown in Fig. 5 The stagnation conditions for Fig. 5 are a temperature of 723 K and a pressure of 30 bar, and the nozzle throat radius is 0.0015 m. The values of the flow velocity and Mach number were compared with those obtained from the analytical study. Fig. 5a shows a comparison of the gas velocity along the axial nozzle coordinates obtained using both methods. Fig. 5b shows the Mach number comparison along the longitudinal axis of the divergent section.

Both methods provided similar gas velocities with the distance from the constriction section. Furthermore, the same trend was observed for the Mach number (Fig. 5b). Hence, the analytical solution of the equations is consistent with the results obtained by the CFD simulation.

4.2. Divergent nozzle geometry

In order to demonstrate an example of the model results, Fig. 6a shows the geometry obtained by the model with a particle velocity at the nozzle throat of 200 m/s for a fixed divergent length of 0.1 m and a nozzle radius of 0.0015 m. The stagnation conditions for these simulations were a pressure of 30 bar and a temperature

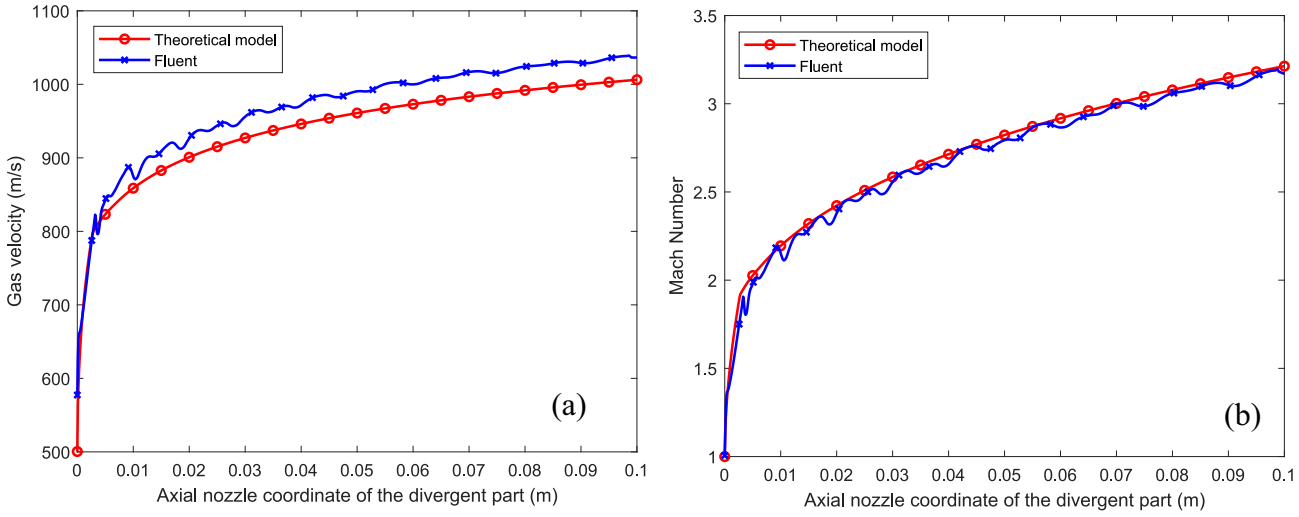

Fig. 5. A comparison between the solutions provided by the theoretical model and a CFD simulation with Fluent in terms of (a) the gas velocity in the divergent part, and (b) the Mach number in the divergent part, for stagnation conditions of 723 K and 30 bar and a nozzle throat radius of 0.0015 m.

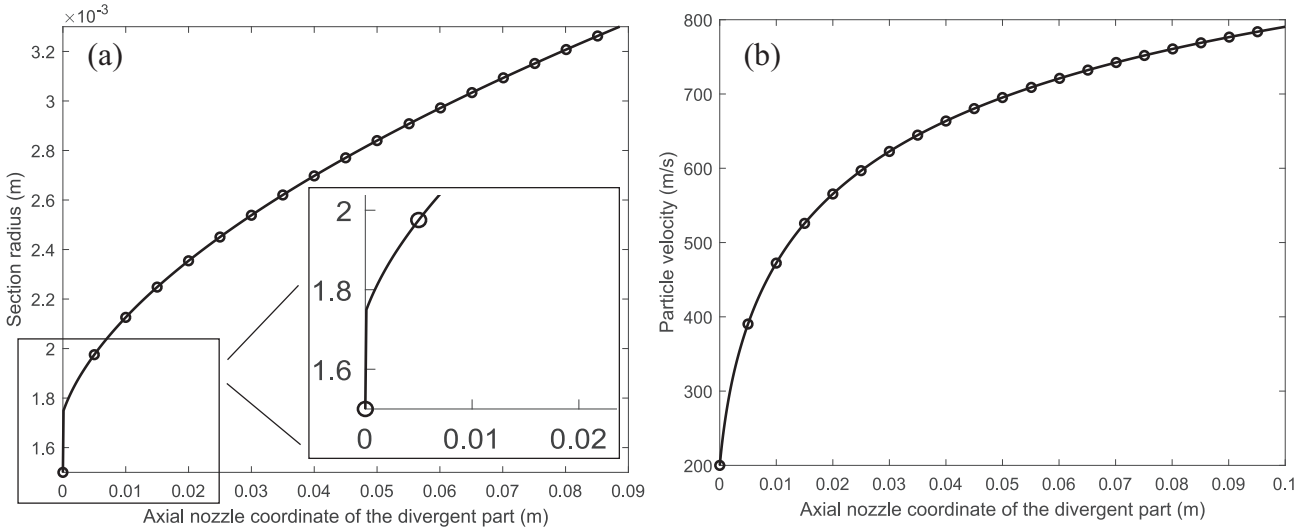

Fig. 6. (a) Section radius, and (b) particle velocity versus axial nozzle coordinate of the divergent part for an initial velocity of 200 m/s and stagnation conditions of 723 K and 30 bar.

of 723 K. Fig. 6b shows the particle velocity along the axial nozzle coordinate of the divergent part.

Fig. 6a depicts the discontinuity from 1.5 mm to the next value at the nozzle throat. However, thereafter, the optimal geometry is represented by a smooth curve with the most appropriate curvature according to the literature [17]. Fig. 6b shows that the particle velocity curve exhibits a monotonous growth. From half the divergent part, the particle velocity barely increases its value by 13%. This detail can help the manufacturers obtain an optimal solution regarding the particle velocity and the material used for the nozzle divergent part. In this regard, an analysis of the influence of the divergent nozzle length is presented in the next subsection.

The angle restriction is added to avoid the discontinuity shown in Fig. 6a. For this purpose, three different geometries with maximum angle restrictions of $2^{\circ}, 5^{\circ}$, and 8°, always below the maximum of 10° were imposed based on the designs recommended in the literature [18]. The results of the optimal geometries under these restrictions are shown in Figure 7a. Nevertheless, there is still a discontinuity in the derivative of the section radius with respect to the axial nozzle coordinate, which may negatively affect the gas flow. To overcome this drawback, a smooth transition was defined between the two regimes as follows: first, the derivatives were calculated to the right and left of the transition point at a distance which is 1% of the total divergent length. Subsequently, the new section radii are calculated within this regime, ensuring linear growth of the derivatives. This modification is evident in Fig. 7b, although the change is subtle. Thus, the plot of the section radius versus the axial nozzle coordinate becomes a smooth curve. The discontinuities in the derivatives are overcome, and a correct gas flow is ensured. Furthermore, the final velocity was not affected by the small region in which the smooth transition was defined.

Fig. 7 confirms that the differences between the section for 5° and 8° is negligible. Thus, it can be inferred that there is a limiting angle for each divergent nozzle length and stagnation conditions

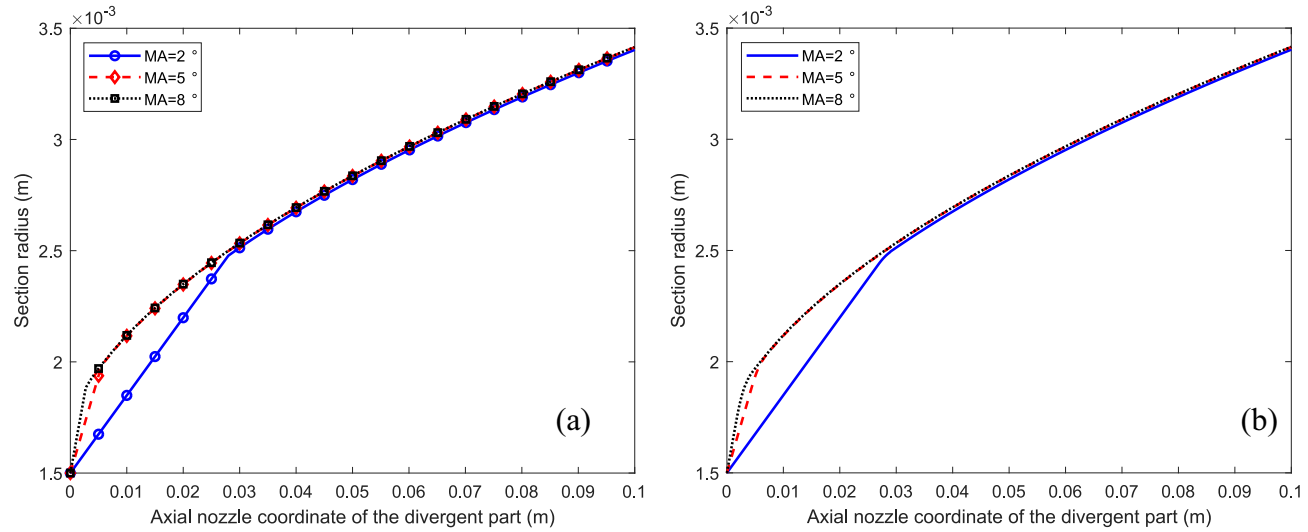

Fig. 7. Section radius, (a) without and (b) with the smooth transition region, of the optimal geometry with different angle restrictions of 2○, 5○ and 8○ versus axial nozzle coordinate of the divergent part for an initial velocity of 200 m/s and stagnation conditions of 723 K and 30 bar.

beyond which the optimal geometry is not sensitive. Further analyses are presented in the next section to give more insights into the subject.

Moreover, a comparison between a regular commercial conical shape and the optimised shape is made in terms of the particle velocity to measure the improvement and utility of the model. The corresponding results for the particle velocity versus the axial nozzle coordinate of the divergent part for the three geometries are represented in Fig. 8.

Fig. 8 shows that the particle velocity is almost identical for all the cases analysed. However, the conical shape always provides particle velocities below the results given by the optimal shapes. Nevertheless, these results may not be comprehensive. To further investigate the observations, a conical shape was built with the throat and exit diameters same as given by the theoretical model. Thus, to determine the influence of the conical shape on the particle velocity, the exit particle velocity as a function of the exit diameter–throat diameter ratio is represented in Fig. 9.

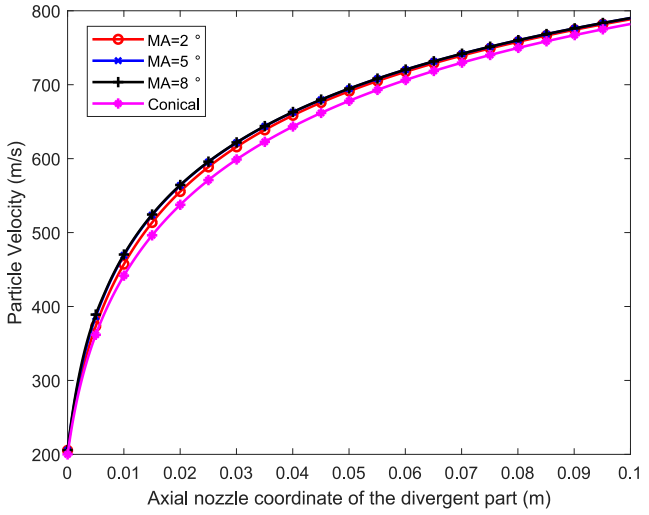

Fig. 8. Particle velocity provided by the optimal geometry with angle restrictions of 2○, 5○ and 8○ as well as the commercial conical shape versus the axial nozzle coordinate of the divergent part for an initial velocity of 200 m/s and stagnation conditions of 723 K and 30 bar.

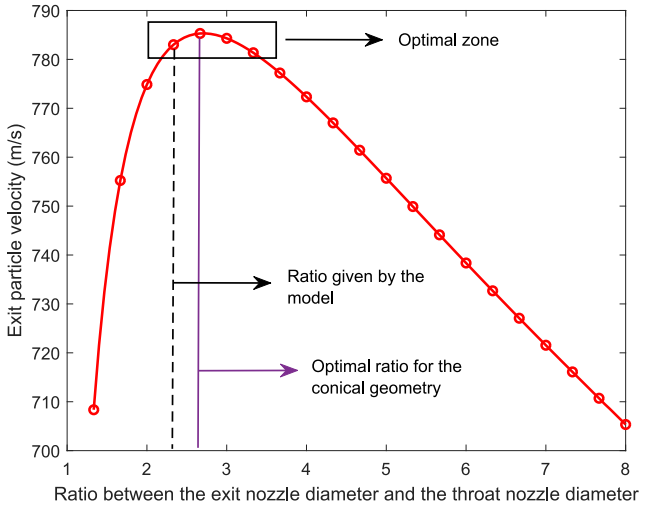

Fig. 9. Exit particle velocity provided by the conical geometry versus the ratio between the exit nozzle diameter and the throat nozzle diameter for an initial velocity of 200 m/s and stagnation conditions of 723 K and 30 bar.

Fig. 9 indicates that there is an optimal range of diameter ratios—approximately from 2 to 3.5—that maximises the exit particle velocity for a conical geometry. If the diameter ratio lies outside this range, the differences between the optimal and conical shapes are remarkable. The exit particle velocity obtained is always below that provided by the analytical model (790 m/s). This implies that the theoretical model not only affords the geometry that maximises the particle velocity but also provides a relationship of diameters within the optimal zone in terms of the exit particle velocity for a conical geometry. This remarkable result is valuable for obtaining a simple conical geometry that is easy to manufacture.

4.3. Parametric study of the optimal variables of interest

As detailed in the previous section, a study to quantify the influence of the maximum permissible angle and the length of the divergent part on the exit particle velocity was performed. All the analyses were performed for the optimal geometry in this section. Fig. 10a shows the resulting surface by representing the exit particle velocity for each length of the divergent part and the maximum permissible angle. For better understanding of Fig. 10a, Fig. 10b shows the corresponding contour plots for constant exit particle velocities.

Fig. 10b indicates that the maximum permissible angle slightly influences the exit velocity up to a maximum angle of 2° for a constant length of the divergent part. Beyond 2°, the exit particle velocity is completely independent of the angle restriction. This is in agreement with the findings in Fig. 7, where the optimal geometry barely changes between 5° and 8°. Furthermore, the contour plots shown in Fig. 10b indicate that the exit particle velocity increases as long as the length of the divergent part increases. This is in concordance with Fig. 6b where the derivative of the particle velocity with respect to the axial nozzle coordinate of the divergent part is smaller as long as the distance to the nozzle throat is increased. This result reveals that the first part of the divergent nozzle length is responsible for most of the particle acceleration.

Another important goal is to determine the stagnation pressure and temperature required for a specific optimal geometry to achieve a certain exit particle velocity. Fig. 11 shows an example of the exit particle velocity as a function of the stagnation temperature and pressure for a velocity of 200 m/s at the nozzle throat, a divergent part length of 0.1 m, and a maximum angle of 5°. This plot is particularly useful in cold-spray equipment, which has limited range of stagnation pressures and temperatures. For instance, if the pressure is limited to a small range, as shown in Fig. 11b the temperature needed to achieve a certain exit velocity can be easily determined.

Fig. 11b indicates that the pressure and temperature are inversely proportional. Thus, to maintain an exit particle velocity, if the stagnation pressure decreases, the stagnation temperature must be increased, and vice versa. The shape of the contour plots remained hyperbolic within the studied range. Finally, the theoretical model developed in this study can be used to optimise the geometric parameters of the divergent part of the nozzle, such as the length and the exit diameter, to obtain a certain exit particle velocity for a known velocity at the nozzle throat. In this regard, Fig. 12 shows the exit particle velocity as a function of the length of the divergent part and the particle velocity at the nozzle throat for low pressure (4 bar and 723 K, Fig. 12a), medium pressure

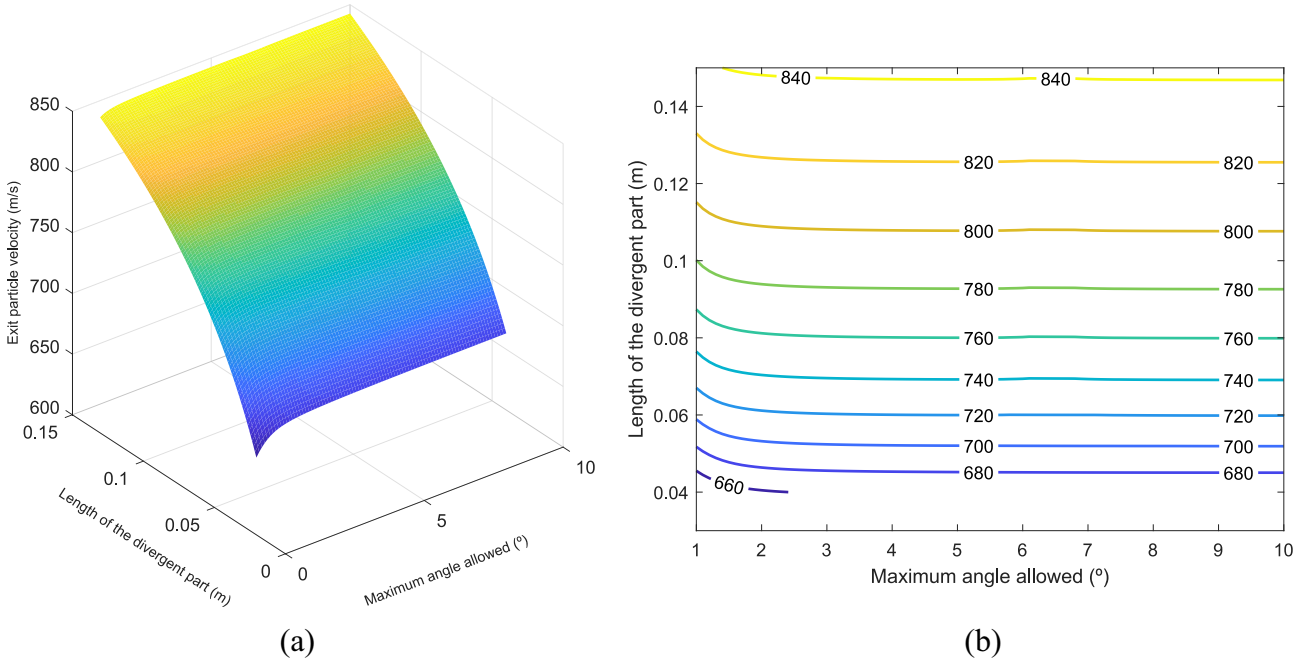

Fig. 10. (a) Exit particle velocity and (b) the corresponding contour plots as a function of the divergent part length and the maximum permissible angle at stagnation temperatures and pressures of 723 K and 30 bar respectively and a 0.0015 m nozzle radius.

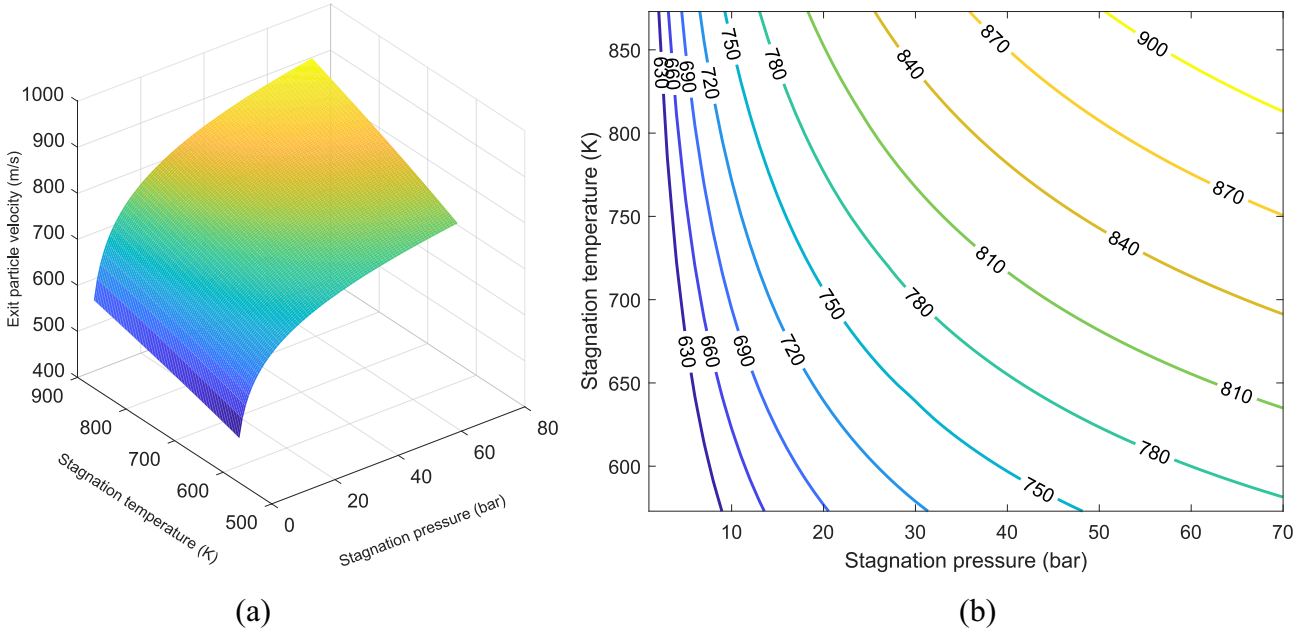

Fig. 11. (a) Exit particle velocity and (b) the corresponding contour plots as a function of the stagnation pressures and temperatures for a velocity of 200 m/s at the nozzle length, a length of 0.1 m for the divergent part and a maximum allowed angle of 5○.

(30 bar and 723 K, Fig. 12b), and high pressure (60 bar and 723 K, Fig. 12c). In addition, the corresponding contour plots of the exit particle velocity and the ratio between the exit and the nozzle throat diameters are presented in Fig. 12d, 12e, 12f, and Fig. 12g, 12 h, 12i, respectively. Thus, the most important geometric features are determined on the basis of the length of the divergent part and the particle velocity at the nozzle throat.

Fig. 12d, 12e and 12f illustrate that the exit particle velocity is not considerably sensitive to the particle velocity at the nozzle throat, practically independent for stagnation pressures of 30 bar and 60 bar. For low pressure (Fig. 12d) it is slightly dependent on the particle velocity at the nozzle throat, being higher if this parameter is higher. This outcome justifies the paucity of studies concerning the convergent part of the nozzle. If the Mach number

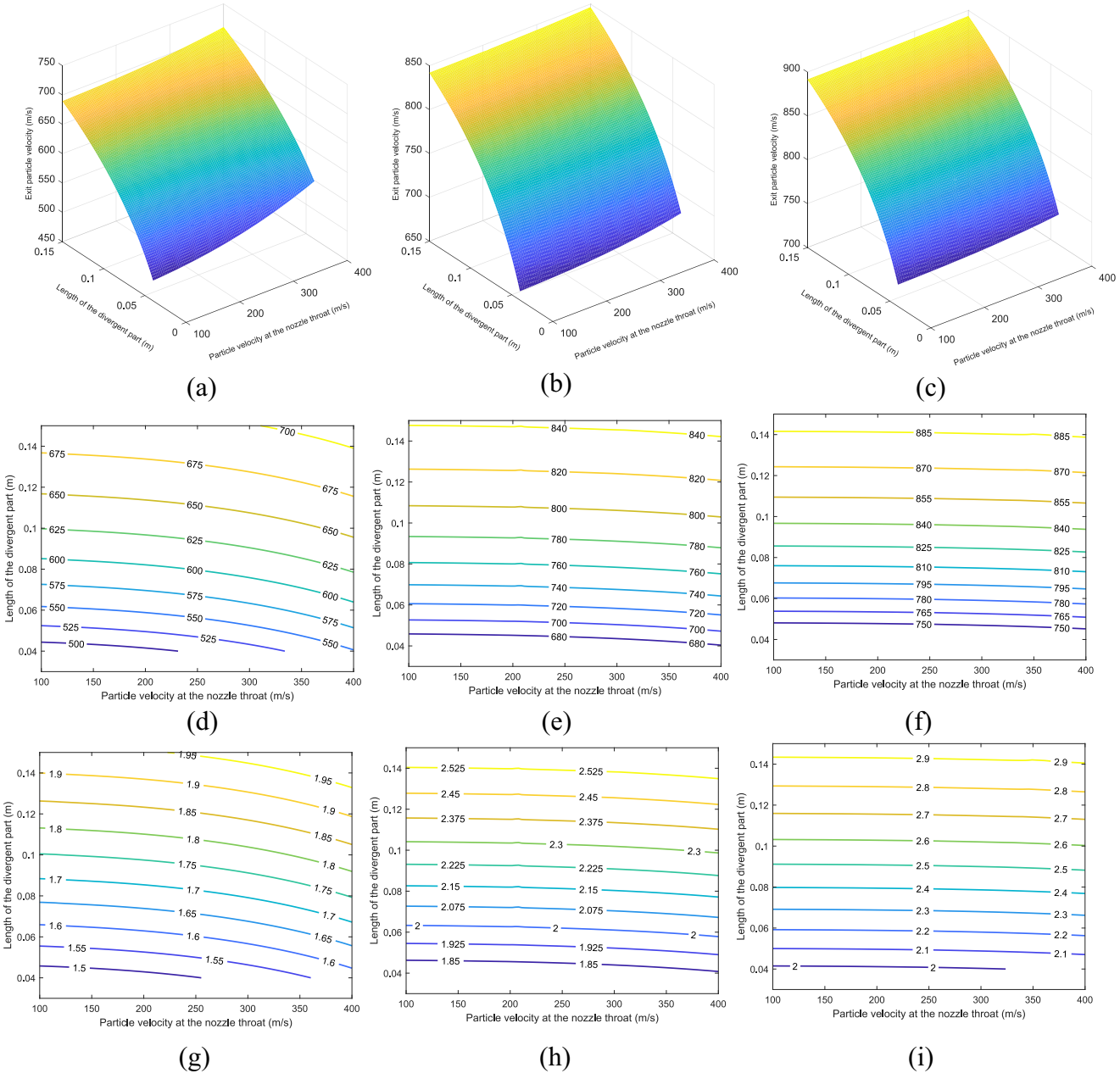

Fig. 12. (a),(b),(c) Exit particle velocity, (d),(e),(f) the corresponding contour plots, and (g),(h),(i) ratio between the exit nozzle diameter and the nozzle throat diameter, as a function of the length of the divergent part and the particle velocity at the nozzle throat for stagnation pressures and temperatures of (a),(d),(g) 4 bar (b),(e),(h) 30 bar (c),(f),(i) 60 bar and 723 K, and a maximum permissible angle of 5°.

is always 1 at the nozzle throat and the exit particle velocity does not vary with the velocity at this point, the geometry of the convergent part is apparently not a significant feature. Fig. 12d, 12e, 12f also show that the exit particle velocity increases slower as long as the length of the divergent part is increased. This behaviour is in agreement with Fig. 10b. Fig. 12g, 12 h and 12i predict the same trends for the ratio between the exit diameter and the throat diameter as Fig. 12d, 12e and 12f for the exit particle velocity.

To elucidate the influence of the two key parameters, namely the particle size and material, on the outcome of the model, a comparison among four extreme cases was performed. The optimal geometry obtained using the model is illustrated in case of aluminium ($\rho = 2800$ kg/m^3) and steel ($\rho = 7800$ kg/m^3) particles with diameters of 10 μm and 100 μm in Fig. 13.

The first result inferred from Fig. 13 is that lighter particles (aluminium, in this case) lead to larger exit diameters and consequently in more open geometries at constant particle diameters. In addition, the smaller the particle size, the larger are the exit diameters of the same material. Another interesting finding is the larger variation in the exit diameters when varying the particle size for lighter materials. In Fig. 13, the variation in the geometry is more important for aluminium when the particle diameter increases from 10 μm to 100 μm. These results confirm the strong correlation between the optimal geometry and the material and particle size used. Therefore, to ensure optimal results in terms of the particle velocity, it is necessary to obtain a unique nozzle shape for each particle diameter, material, and stagnation conditions.

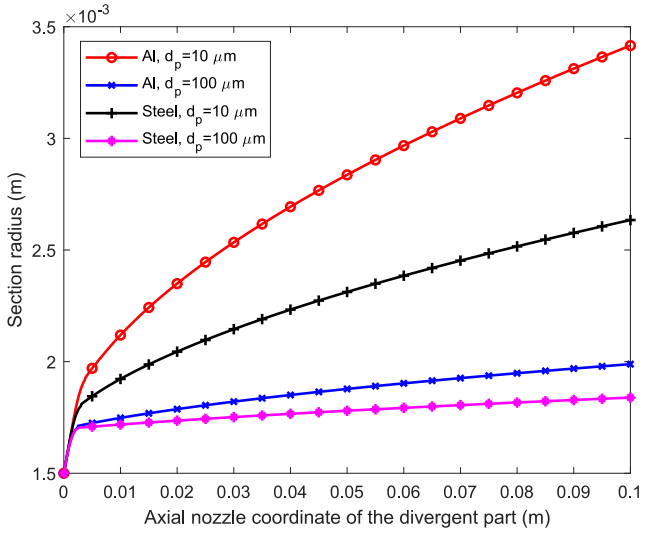

Fig. 13. Section radius versus axial nozzle coordinate of the divergent part for four different cases: aluminium withd_p = 10 μm andd_p = 100 μm; and steel withd_p = 10 μm; d_p=100 μm for an initial velocity of 200 m/s and stagnation conditions of 723 K and 30 bar.

5. Conclusions

A new optimisation model based on the one-dimensional isentropic theory to obtain the optimal geometry of the nozzle divergent part for the cold-spray process was developed in this study. The model was formulated using the Lagrange multiplier method to maximise the drag force on the particle at each integration step by searching for the optimal Mach number and, consequently, the optimal geometry. A major novel aspect of the model is the introduction of a useful geometric criterion to avoid mathematical discontinuity in the geometry at the nozzle throat.

The limitations of the common hypotheses widely used in the particle motion equation were analysed. A comparison between the traditional models and a model which considers all dependencies for the integration of the motion equation was performed. For the different sets of stagnation pressures and temperatures studied, the results of the exit particle velocity presented a considerably low error in the simplified model (below 10%). Nevertheless, for certain conditions, the errors were greater than 15%. Because this model was intended to be used within a wide range of stagnation conditions, the full integrated model with all the dependencies considered was selected.

A set of optimal geometries were obtained with different maximum angle restrictions to avoid geometric discontinuities. To prevent occurrence of a new discontinuity due to the change of shape caused by the dominant role of the Lagrange multiplier method, instead of the geometric restriction up to a certain axial coordinate, a criterion of linear continuity in the derivatives was applied to make the curve sufficiently smooth and avoid related issues with the gas flow. In addition, a parametric study of the optimal variables of interest was performed. From this study, it can be inferred that the restriction of the maximum permissible angle does not significantly change the exit particle velocity from 2○, and that the region near the nozzle throat is the most critical part of the particle acceleration in view of the contour plots. In addition, a comparison with a conical shape was performed, revealing that if the optimal exit diameter/throat diameter ratio is maintained, a solution close to the optimal can be obtained with the appropriate conical geometry. Moreover, the stagnation pressures and temperatures showed a hyperbolic dependency to obtain the same exit particle velocity for a fixed nozzle length and angle restriction. The particle velocity at the nozzle throat only slightly influenced the exit particle velocity and the exit nozzle diameter for the low-pressure case, showing that the convergent part does not remarkably affect the optimal parameters of the divergent part. Finally, from the study with different materials and particle sizes, it can be concluded that the smaller the particle size and the lighter the material used, the larger is the exit diameter of the optimal geometry.

Declaration of Competing Interest

The authors declare that they have no known competing financial interests or personal relationships that could have appeared to influence the work reported in this paper.

Acknowledgements

The authors would like to acknowledge the financial support received from the Spanish government AEI under Grant No. PID2020-115508RB-C22 (A3M). The authors are also grateful to URJC for its support of the Cold-SAM project.

References

[1] A. Alkhimov, V. Kosarev, A. Papyrin, A method of cold gas dynamic deposition, Dokl. Akad. Nauk SSSR 315 (1990) 1062–1065.
[2] A. Alkhimov, A. Papyrin, V. Dosarev, N. Nestorovich, M. Shuspanov, Gas dynamic spraying method for applying a coating, US Pat. 5,302,414.
[3] H. Assadi, F. Gärtner, T. Stoltenhoff, H. Kreye, Bonding mechanism in cold gas spraying, Acta Mater. 51 (15) (2003) 4379–4394, https://doi.org/10.1016/S1359-6454(03)00274-X.
[4] H. Assadi, T. Schmidt, H. Richter, J.-O. Kliemann, K. Binder, F. Gärtner, T. Klassen, H. Kreye, On parameter selection in cold spraying, J. Therm. Spray Technol. 20 (6) (2011) 1161–1176, https://doi.org/10.1007/s11666-011-9662-9.
[5] S. Buhl, P. Breuninger, S. Antonyuk, Optimization of a laval nozzle for energy-efficient cold spraying of microparticles, Mater. Manuf. Process. 33 (2018) 115–122, https://doi.org/10.1080/10426914.2017.1279322.
[6] V. Champagne, D. Helfritch, S. Dinavahi, P. Leyman, Theoretical and experimental particle velocity in cold spray, J. Therm. Spray Technol. 20 (2011) 425–431, https://doi.org/10.1007/s11666-010-9530-z.
[7] R. Clift, J. Grace, M. Weber, Bubbles, Drops, and Particles, Academic Press, New York, 1978.
[8] M. Diab, X. Pang, H. Jahed, The effect of pure aluminum cold spray coating on corrosion and corrosion fatigue of magnesium (3% al-1% zn) extrusion, Surf. Coat. Technol. 309 (2017) 423–435, https://doi.org/10.1016/j.surfcoat.2016.11.014.
[9] R. Dykhuizen, R. Neiser, Optimizing the cold spray process, in: F.L. Orlando (Ed.), Advancing the Science and Applying the Technology 1, May 5–8, ASM International, 2003, pp. 19–26.
[10] R. Dykhuizen, M. Smith, Gas dynamic principles of cold spray, J. Therm. Spray Technol. 7 (1998) 205–212, https://doi.org/10.1361/105996398770350945.
[11] D. Gilmore, R. Dykhuizen, R. Neiser, T. Roemer, M. Smith, Particle velocity and deposition efficiency in the cold spray process, J. Therm. Spray Technol. 8 (1999) 576–582, https://doi.org/10.1361/105996399770350278.
[12] M. Grujicic, C. Tong, W.S. DeRosset, D. Helfritch, Flow analysis and nozzle-shape optimization for the cold-gas dynamic-spray process, Proc. Inst. Mech. Eng. Part B J. Eng. Manuf. 217 (11) (2003) 1603–1613, https://doi.org/10.1243/095440503771909980.
[13] M. Grujicic, C.L. Zhao, C. Tong, W.S. DeRosset, D. Helfritch, Analysis of the impact velocity of powder particles in the cold-gas dynamic-spray process, Mater. Sci. Eng., A 368 (1-2) (2004) 222–230, https://doi.org/10.1016/j.msea.2003.10.312.
[14] C.B. Henderson, Drag coefficients of spheres in continuum and rarefied flows, AIAA J. 14 (6) (1976) 707–708, https://doi.org/10.2514/3.61409.
[15] B. Jodoin, Cold spray nozzle match number limitation, J. Therm. Spray Technol. 11 (2001) 496–507, https://doi.org/10.1361/105996302770348628.
[16] H. Koivuluoto, J. Larjo, D. Marini, G. Pulci, F. Marra, Cold-sprayed al6061 coatings: Online spray monitoring and influence of process parameters on coating properties, Coatings 10 (4) (2020) 348, https://doi.org/10.3390/coatings10040348.
[17] C. Li, W. Li, H. Liao, W. Li, C.J. Li, Optimal design of a novel cold spray gun nozzle at a limited space, J. Therm. Spray Technol. 14 (2005) 391–396, https://doi.org/10.1361/105996305X59404. Li, W., Liao, H., Wang, H.
[18] W.-Y. Li, H. Liao, H.-T. Wang, C.-J. Li, G.a. Zhang, C. Coddet, Optimal design of a convergent-barrel cold spray nozzle by numerical method, Appl. Surf. Sci. 253 (2) (2006) 708–713, https://doi.org/10.1016/j.apsusc.2005.12.157.
[19] W.-Y. Li, H. Liao, G. Douchy, C. Coddet, Optimal design of a cold spray nozzle by numerical analysis of particle velocity and experimental validation with 316l

stainless steel powder, Mater. Des. 28 (7) (2007) 2129–2137, https://doi.org/10.1016/j.matdes.2006.05.016.
[20] K. Ling, W. McCain, E. Davani, G. Falcone, Measurement of gas viscosity at high pressures and high temperatures, Int. Petrol. Technol. Conf. (2009), https://doi.org/10.2523/IPTC-13528-MS.
[21] R. Lupoi, W. O'Neill, Powder stream characteristics in cold spray nozzles, Surf. Coat. Technol. 206 (6) (2011) 1069–1076, https://doi.org/10.1016/j.surfcoat.2011.07.061.
[22] T. Marrocco, D.G. McCartney, P.H. Shipway, A.J. Sturgeon, Production of titanium deposits by cold-gas dynamic spray: Numerical modeling and experimental characterization, J. Therm. Spray Technol. 15 (2) (2006) 263–272, https://doi.org/10.1361/105996306X108219.
[23] P. Poza, M.Á. Garrido-Maneiro, Cold-sprayed coatings: Microstructure, mechanical properties, and wear behaviour, Prog. Mater Sci. 123 (2022) 100839, https://doi.org/10.1016/j.pmatsci.2021.100839.
[24] K. Sakaki, S. Shinkai, N. Ebara, Y. Shimizu, Effect of gun nozzle geometry, increase in the entrance convergent section length and powder injection position on cold sprayed titanium coatings, Mater. Sci. Forum 534–536 (2007) 413–416, https://doi.org/10.4028/www.scientific.net/MSF.534-536.413.
[25] B. Samareh, A. Dolatabadi, Dense particulate flow in a cold gas dynamic spray system, ASME, San Diego, CA, United States, 2007a, pp. 881–889. doi: 110.1115/FEDSM2007-37283.
[26] B. Samareh, A. Dolatabadi, A three-dimensional analysis of the cold spray process: The effects of substrate location and shape, J. Therm. Spray Technol. 16 (5-6) (2007) 634–642, https://doi.org/10.1007/s11666-007-9082-z.
[27] P. Sirvent, M. Garrido-Maneiro, C. Munez, P. Poza, S. Vezzu, Effect of higher deposition temperatures on the microstructure and mechanical properties of al 2024 cold sprayed coatings, Surf. Coat. Technol. 337 (2018) 461–470, https://doi.org/10.1016/j.surfcoat.2018.01.055.
[28] T. Stoltenhoff, H. Kreye, H. Richter, H. Assadi, Optimization of the cold spray process, Singapore (2001) 409–416.
[29] T. Stoltenhoff, H. Kreye, H.J. Richter, An analysis of the cold spray process and its coatings, J. Therm. Spray Technol. 11 (2002) 542–550, https://doi.org/10.1361/105996302770348682.
[30] T. Stoltenhoff, J. Voyer, H. Kreye, Cold spraying – state of the art and applicability kaltgasspritzen – stand der technik und anwendungsmöglichkeiten, in: International Thermal Spray Conference, March 4–6, Essen, Germany, DVS Deutscher Verband föur Schweißen, 2002, pp. 366–374.
[31] S. Vadla, J. Doom, Analysis of jet characteristics among various cold spray nozzle, J. Therm. Spray Technol. 1 (2018) 24–31, https://doi.org/10.52687/2582-1474/115.
[32] P. Wright, The variation of viscosity with temperature, Phys. Educ. 12 (1977).
[33] S. Yin, M. Meyer, W. Li, H. Liao, R. Lupoi, Gas flow, particle acceleration, and heat transfer in cold spray: A review, J. Therm. Spray Technol. 25 (2016) 874–896, https://doi.org/10.1007/s11666-016-0406-8.
[34] Wen-Ya Li, Chang-Jiu Li, Optimal design of a novel cold spray gun nozzle at a limited space, Journal of Thermal Spray Technology 14 (3) (2005) 391–396, https://doi.org/10.1361/105996305X59404.